



High lithium storage capacity and rate capability achieved by mesoporous Co_3O_4 hierarchical nanobundles

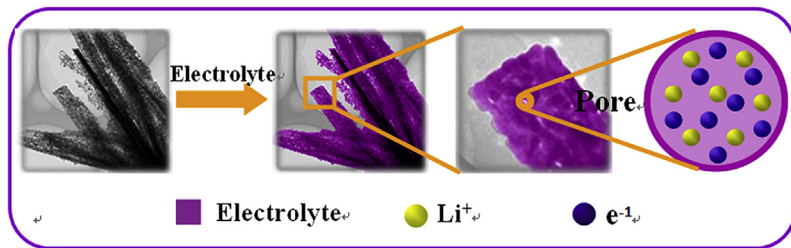
Ying Xiao, Changwen Hu, Minhua Cao*

Key Laboratory of Cluster Science, Ministry of Education of China, Department of Chemistry, Beijing Institute of Technology, Beijing 100081, PR China

HIGHLIGHTS

- Mesoporous Co_3O_4 hierarchical nanobundles were successfully synthesized.
- This structure is beneficial for the transport kinetics for Li^+ and electron.
- They exhibit high specific capacity and high-rate performance.

GRAPHICAL ABSTRACT



ARTICLE INFO

Article history:

Received 8 June 2013

Received in revised form

15 August 2013

Accepted 17 August 2013

Available online 2 September 2013

Keywords:

Cobalt oxide

Mesoporous

Hierarchical

Nanobundles

Anode

Lithium-ion batteries

ABSTRACT

In this work, we report the feasibility to achieve high lithium storage capacity and rate capability of Co_3O_4 anode materials by preparing hierarchically mesoporous structure. The resultant mesoporous Co_3O_4 hierarchical nanobundles exhibit a high specific capacity and favorable high-rate performance when used as an anode material for lithium ion batteries (LIBs). The reversible specific capacity could be kept at 1667.6 mAh g⁻¹ at a current density of 0.1 A g⁻¹ after 60 cycles. Even at high current densities of 1 A g⁻¹ and 5 A g⁻¹, the Co_3O_4 electrodes still could deliver a remarkable discharge capacity of 1264.8 and 603.0 mAh g⁻¹ after 100 cycles, respectively. The unique mesoporous hierarchical structure should be responsible for the superior electrochemical performance. The good rate capability demonstrates the mesoporous Co_3O_4 hierarchical nanobundles have a great potential as a high-rate anode material in LIBs.

© 2013 Elsevier B.V. All rights reserved.

1. Introduction

As an important energy storage device, lithium ion batteries (LIBs) have received much attention in various fields such as electric vehicles (EV) and hybrid electric vehicle (HEVs), owing to their advantages of high energy density and power density as well as long cycle life [1–4]. However, the conventional LIBs fall far behind the fast-growing requirements for higher specific power density and higher rate capability. Therefore, developing new electrode

materials with improved energy density and rate performance is a major challenge [5,6]. Among all possible anode materials, 3d transition-metal oxides such as NiO , Co_3O_4 (CoO), and Fe_2O_3 (Fe_3O_4) are relatively cheap, easily available and high-capacity [7]. Especially, Co_3O_4 has been given special attention since Co_3O_4 anodes could operate at higher voltage and offer a much higher theoretical capacity (890 mAh g⁻¹), which is about 2.4 times larger than that of the graphite (372 mAh g⁻¹). However, similar to other high capacity materials, Co_3O_4 also suffers from large volume changes and severe particle aggregation during charge–discharge cycles, which inevitably leads to electrode pulverization and a loss of inter-particle electronic contact and consequently a large irreversible capacity loss and poor cycling stability [8,9]. To solve these

* Corresponding author.

E-mail address: caomh@bit.edu.cn (M. Cao).



problems, two main strategies have been developed to improve Co_3O_4 anode performance. For example, Co_3O_4 has been combined with conductive materials such as amorphous carbon and graphene, which indeed could improve the electrode performance to some extent [10–12]. However, this strategy often leads to the decrease of the total capacity of the electrode due to the presence of low-capacity carbon. Another appealing and effective strategy is to tailor special microstructures of Co_3O_4 (such as porous structures and nanowire arrays), which can evidently enhance the overall electrode behavior [13–19]. Basically speaking, this strategy is to optimize electrode structure considering the electrochemical reaction at the electrode surface to achieve better electrochemical performance.

Porous nanostructured materials have recently received particular attention due to their wide applications such as gas sensors, catalysis, adsorption, solar cells, LIBs and so on [20–24]. Compared to their bulk counterparts, porous materials show great advantages in terms of high surface area, well-defined morphology and size, and porous texture, which make them exhibit remarkable physical properties. Therefore, many porous nanostructured materials have been intensively studied in various areas due to their potential applications [25–29]. When used as electrode materials for LIBs, porous nanostructured materials will display improved lithium storage properties such as capacity, rate performance and cyclability. On the one hand, the porous nanostructured materials permit Li ions to easily diffuse into the electrode, leading to a high flux of lithium ions across the interface between the electrode and electrolyte. On the other hand, the porous structure could effectively shorten the diffusion pathway of lithium ions and electrons in the as-obtained material electrode and increase the electrochemical reaction area, and at the same time it also could provide space for volume shrinking and expansion during the discharge–charge processes [30–34]. For instance, Lou et al. recently reported the fabrication of CoMn_2O_4 hollow microcubes by thermal decomposition of $\text{Co}_{0.33}\text{Mn}_{0.67}\text{CO}_3$ and the hollow microcubes exhibit a high specific capacity and good cycling performance [27]. Furthermore, Chen's group has also reported CoMn_2O_4 hierarchical microspheres assembled with porous nanosheets and the interconnected pores on the surface of the nanosheets make the sample

achieve a good cycle ability and high rate capability [28]. In addition, three dimensional (3D) porous V_2O_5 microstructures have been successfully synthesized by Lou et al. via a template-free solvothermal method and the as-obtained V_2O_5 delivers a high discharge capacity of 267 mAh g^{-1} at a current density of 300 mA g^{-1} [29].

In view of the superiority of porous structure, we herein demonstrate the fabrication of mesoporous Co_3O_4 hierarchical nanobundles by a facile hydrothermal strategy along with subsequent annealing treatment. Fig. 1a schematically illustrates the synthesis strategy. The first step leads to the formation of a precursor with a bundle-like morphology and the second step involves thermal decomposition of the precursor under air, resulting in the formation of mesoporous Co_3O_4 hierarchical nanobundles. During this thermal decomposition process, besides that the bundle-like morphology is completely maintained, mesoporous structure is synchronously generated due to thermally driven contraction force. When used as anode materials for LIBs, this unique structure could maximize the availability of the electrochemically active surface area and facilitate the diffusion of lithium ions and electrons as well as the alleviation of volume expansion during the discharge–charge processes. As expected, the mesoporous Co_3O_4 hierarchical nanobundles exhibit an ultrahigh reversibly capacity of about $1264.8 \text{ mAh g}^{-1}$ at a current density of 1 A g^{-1} for 100 cycles and an excellent rate performance (about 367 mAh g^{-1} at a current density of 20 A g^{-1}).

2. Experimental

2.1. Preparation of mesoporous Co_3O_4 hierarchical nanobundles

3 mmol of $\text{Co}(\text{NO}_3)_2 \cdot 6\text{H}_2\text{O}$ (Sinopharm chemical reagent, Beijing Co., Ltd) and 2 g of urea (Sinopharm chemical reagent, Beijing Co., Ltd) were dissolved in 60 mL mixed solvent of ethanol and deionized water with a volume ratio of 1:1. After being magnetically stirred for 10 min, the as-obtained homogeneous solution was transferred into a 80 mL Teflon-lined stainless steel autoclave, sealed and maintained at 180°C for 12 h to yield a precursor. Subsequently, the precursor was collected by centrifugation and

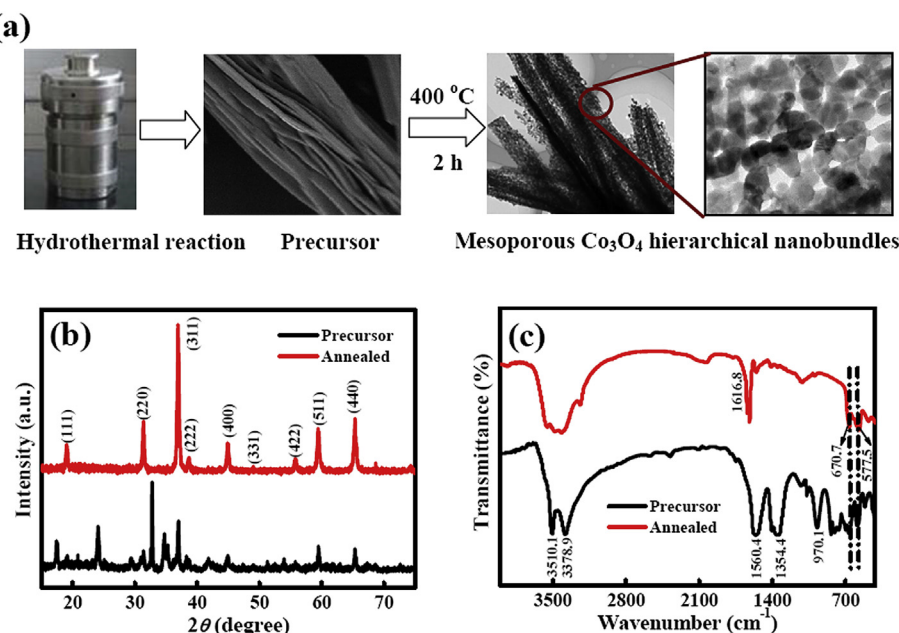


Fig. 1. (a) The synthesis strategy of the mesoporous Co_3O_4 hierarchical nanobundles. (b) XRD patterns and (c) FT-IR spectra of the precursor and the annealed product.

washed thoroughly with water. After freeze-drying (Freeze Drier, FD-1C-50) with the temperature and pressure of -50°C and 20 Pa for 24 h, the precursor was annealed at 400°C for 2 h at a heating rate of $2^{\circ}\text{C min}^{-1}$ to yield the final product.

2.2. Characterization

The phase purity of the as-synthesized samples was analyzed by powder X-ray diffraction (XRD) with $\text{Cu K}\alpha$ ($\lambda = 1.54178\text{ \AA}$) incident radiation by a Shimadzu XRD-6000 operated at 40 kV voltage and 50 mA current. XRD pattern was recorded from 15 to 75° (2θ) with a scanning step of $5^{\circ}\text{ min}^{-1}$. The size and morphology of the samples were measured by a H-8100 transmission electron microscopy (TEM) operating at 200 kV accelerating voltage. The field emission scanning electron microscopy (FE-SEM) and the element mapping of the sample were taken on Hitachi S-4800 SEM unit. X-ray photoelectron spectra (XPS) were recorded on an ESCALAB 250 spectrometer (Perkin–Elmer) to characterize the surface composition. Fourier transform infrared (FT-IR) spectra were recorded on a Nicolet 170SXFTIR spectrometer using pressed KBr pellets to test the chemical bonding of the samples. The Brunauer–Emmett–Teller (BET) surface area of as-synthesized samples was measured using a Belsorp-max surface area detecting instrument by N_2 physisorption at 77 K. TG analysis was performed on a DTG-60AH instrument.

2.3. Electrochemical measurements

Electrochemical performance was tested by using coin cells (CR2025) at room temperature on a multi-channel battery testing system (LAND CT2001A) with a cutoff voltage of 3.00–0.01 V vs. Li^+/Li . For the anode preparation, a mixture of active material (sample: acetylene black = 3:1, about 21 wt% acetylene black was used) and binder (Na-alginate, Sinopharm chemical reagent, Beijing Co., Ltd) in a weight ratio of 85:15 was ground in a mortar with deionized water as the solvent to make slurry, and the resultant slurry was then uniformly pasted on a Cu foil current collector. The typical electrode was dried at 120°C for 36 h under vacuum before assembled into coin cell in an argon-filled glovebox. The loading of the slurry electrode was 0.562 mg cm^{-2} . Lithium foil (Guotai-Huangrong, Co., Ltd) was used as the counter electrode and solution of 1 M LiPF_6 in ethylene carbonate (EC)/dimethyl carbonate (DMC)/diethyl carbonate (DEC) (1:1:1 in volume) was used as electrolyte (Guotai-Huangrong, Co., Ltd). Cyclic voltammetry (CV) curves were recorded on a CHI-760E potentiostat at a scanning rate of 0.5 mV s^{-1} at room temperature. The impedance spectra were obtained by applying a sine wave with amplitude of 5 mV over the frequency range from 100 kHz to 0.01 Hz.

3. Results and discussion

3.1. Composition and morphology

The precursor obtained by the hydrothermal process was first examined by X-ray diffraction (XRD). As shown in Fig. 1b (black curve), the precursor is well crystalline, but it is difficult to assign the pattern unambiguously to a specific phase. To further investigate the composition of the precursor, Fourier transform infrared (FT-IR) measurement was carried out, as shown in Fig. 1c. The bands centered at 3378.9 and 3510.1 cm^{-1} can be attributed to the stretching vibration of the O–H bond, $\nu(\text{OH})$. The bands at 1560.4 and 1354.4 cm^{-1} are attributed to the stretching vibrations of $\nu(\text{OCO}_2)$ and $\nu(\text{CO}_3)$ in the carbonate anion, whereas the band at about 970.1 cm^{-1} can be ascribed to the $\delta(\text{Co–OH})$ bending vibration [35,36]. Besides, two bands centered at about 670.7 and

577.5 cm^{-1} also appear, which correspond to the absorption of Co–O [37,38]. Combining the FT-IR result with that of XRD, we can deduce that the precursor may be a mixture containing at least cobalt hydroxycarbonate and Co_3O_4 . After annealing at 400°C for 2 h, the precursor was transformed to a pure phase, as shown in Fig. 1b (red curve in web version). All the diffraction peaks were in agreement with a cubic spinel phase of Co_3O_4 (JCPDS Card no. 43-1003). The main peaks at $2\theta \approx 19.0, 31.3, 36.9, 38.6, 44.9, 55.7, 59.5$ and 65.3° can be assigned to (111), (220), (311), (222), (400), (422), (511) and (440) reflections of cubic Co_3O_4 . No other diffraction peaks corresponding to crystalline byproducts are detected, indicating the high purity of the annealed product. Moreover, from the FT-IR spectrum for the annealed sample, we can see that besides the bands at 3460.1 and 1616.8 cm^{-1} for adsorbed water, only the bands at 670.7 and 577.5 cm^{-1} were observed, which correspond to the absorption of Co–O, further confirming the complete transformation of the precursor [38].

The composition and surface chemical state of the Co_3O_4 sample were further investigated by X-ray photoelectron spectrum (XPS), as shown in Fig. 2a. The binding energy was calibrated using the C 1s photoelectron peak at 284.6 eV as the reference. The C 1s peak detected in the survey spectrum may result from the surface-adsorbed carbonaceous materials originating from air [39] and besides the C 1s peak, only Co and O peaks were detected in the survey XPS spectrum. Fig. 2b shows the high resolution XPS spectrum of Co 2p, which shows two major peaks with binding energy at 780.3 and 795.3 eV, corresponding to the $\text{Co 2p}_{3/2}$ and $\text{Co 2p}_{1/2}$ peaks, respectively. The gap between the two peaks is 15.0 eV, which is a typical characteristic of Co_3O_4 phase; the shake-up satellite peaks (805.1, 803.2 and 787.5 eV) confirm the existence of Co^{2+} [6,40]. The high-resolution spectrum for O 1s in Fig. 2c displays four photoelectron peaks at 530.1, 530.9, 532.0 and 533.0 eV that can be assigned to the lattice oxygen in the spinel Co_3O_4 , the oxygen in cobalt monoxide hydroxide ions, oxygen of the hydroxide ions, and small amount of physically adsorbed water molecules, respectively [6,16]. These results further confirm the formation of pure Co_3O_4 phase. Moreover, the TG curves indicated the successful transformation of the precursor to the Co_3O_4 product and further verify the absence of C in the Co_3O_4 sample (Fig. S1).

Fig. 2d shows the scanning electron microscopy (SEM) image of the as-prepared precursor obtained by hydrothermal treatment. It can be seen that the product is composed of nanobundles, while these nanobundles are assembled by nanobelts with an average length of $5\text{ }\mu\text{m}$ without serious aggregation. After annealing at 400°C for 12 h, the precursor can be completely transformed into pure Co_3O_4 phase, which has been confirmed by above studies. It should be noted that the Co_3O_4 product still maintains the bundle-like morphology of the precursor, indicating that the nanobundles are quite thermally stable (Fig. 2e). The high thermal stability should be attributed to a relatively large thickness of about 200 nm of the nanobelts (inset in Fig. 2d). Energy dispersive X-ray spectroscopy mapping shown in Fig. 2f,g confirms the uniform distribution of Co and O elements within the nanobundles.

Further information about the Co_3O_4 nanobundles was obtained from transmission electron microscopy (TEM). Fig. 3a is the TEM image of a randomly selected nanobundle, which clearly displays that the nanobundle consists of assembled nanobelts with an average diameter of about 200 nm. Higher-magnification TEM images shown in Fig. 3b–d reveal that the Co_3O_4 nanobelt is actually a porous structure, which is composed of many nanoparticles instead of the conventional single-crystalline nanobelts [6,15]. Many irregular pores are uniformly dispersed in the whole nanobelt and the diameters of the pores are in the range of 15–25 nm. The formation of the porous structure in the Co_3O_4 nanobelts can be attributed to the thermally driven contraction process

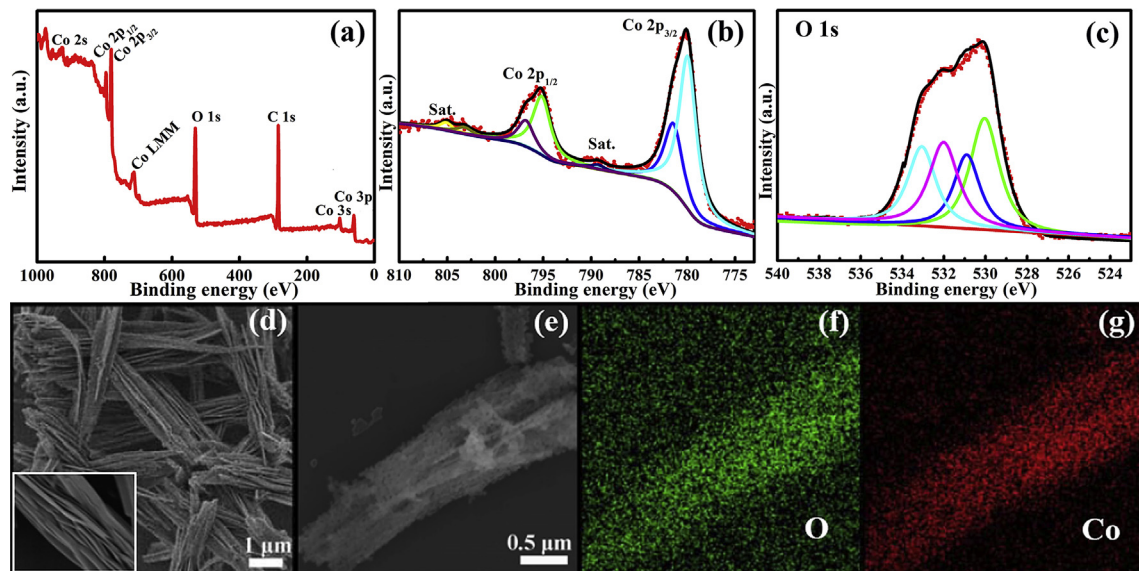


Fig. 2. XPS spectra for the mesoporous Co_3O_4 hierarchical nanobundles: (a) survey spectrum and high resolution spectra for (b) Co 2p and (c) O 1s. The weak peaks around 20 eV in the survey spectrum can be assigned to O 2s and C 2s. (d) SEM image of the precursor. The inset in Fig. 2d is the corresponding magnified FE-SEM image of one part of the precursor. (e–g) SEM image and corresponding EDX element mappings of Co and O for the mesoporous Co_3O_4 hierarchical nanobundles.

during the thermal decomposition of the precursor accompanied with the release of CO_2 and H_2O and this phenomenon is often observed in many reports [16,41,42]. The high-resolution images are recorded on a randomly selected nanoparticle (marked with rectangle 1) and the surrounding area of a well-defined pore (marked with rectangle 2), as shown in Fig. 3e,f. They both show two sets of lattice fringes with interplane spacings of 0.285 and 0.462 nm, respectively, corresponding to the (222) and (111) planes of cubic Co_3O_4 phase. This result suggests that the porous Co_3O_4 nanobelts are highly crystalline.

3.2. Porous properties and electrochemical performance

The porosity of the Co_3O_4 hierarchical nanobundles is further characterized by N_2 adsorption-desorption measurement performed at 77 K. As shown in Fig. 4, the N_2 adsorption isotherms displays a type IV isotherm having a large hysteresis loop at a pressure range of 0.8–1.0 P/P_0 , suggesting the presence of mesopores in the product. Moreover, when the relative pressure is close to 1, the amount of the adsorbed N_2 rapidly increases, indicating that macropores also exist in the Co_3O_4 hierarchical nanobundles.

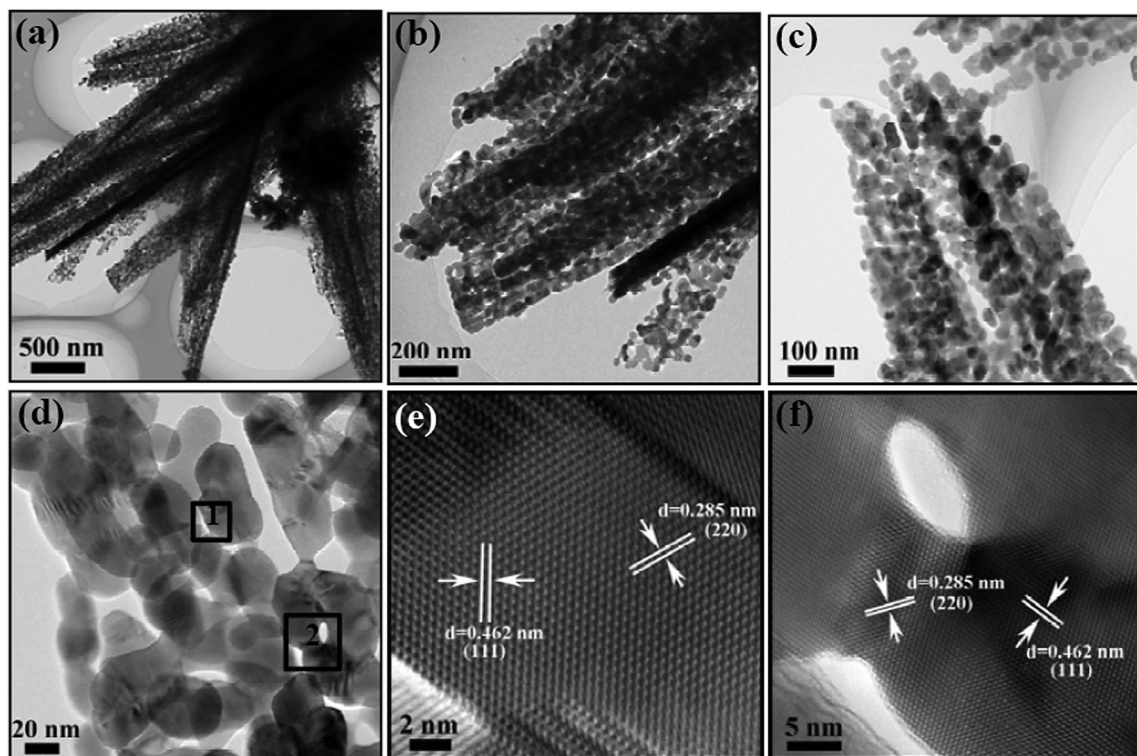
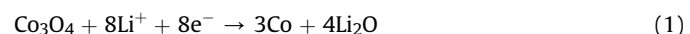


Fig. 3. (a–d) TEM images of the mesoporous Co_3O_4 hierarchical nanobundles. (e,f) High-resolution TEM images of the mesoporous Co_3O_4 hierarchical nanobundles.

We deduce that the release of gases (CO_2 and H_2O) during thermal treatment leads to small pores in nanobelts, whereas the large pores can be attributed to the open space between neighboring nanobelts, and meanwhile, some of the small pores may connect with each other, also generating larger pores. The pore size distribution by the Barrett–Joyner–Halenda (BJH) method is shown in Fig. 4 (inset), and it can be seen that the mesoporous Co_3O_4 hierarchical nanobundles have a wide pore size distribution with an average size of about 22.0 nm, which is in well agreement with that from TEM. Moreover, the Brunauer–Emmett–Teller (BET) surface area is calculated to be $26.4 \text{ m}^2 \text{ g}^{-1}$. It has been well addressed that this kind porous structure will be beneficial for improving the electrochemical performance. Possible reason may be that the pore channel will allow for more facile Li^+ transport in the electrolyte, thus resulting in a better contact of the electrolyte with the electrode. As a consequence, high capacity and rate capability will be obtained accordingly [30–34].

In view of the aforementioned advantages of porous nanostructures as electrode materials in LIBs, we investigate the lithium storage properties of as-prepared mesoporous Co_3O_4 hierarchical nanobundles. Fig. 5a shows galvanostatic charge–discharge curves of the electrodes made from the mesoporous Co_3O_4 hierarchical nanobundles at a current density of 0.1 A g^{-1} in a potential window of 0.01 and 3.0 V (vs. Li^+/Li). Here, lithiation was expressed as discharging, whereas delithiation was expressed as charging. Similar to previous reports [9,34–44], the first discharge voltage profile displays a long flat voltage plateau at about 1.1 V and then gradually decrease to 0 V, which may be a typical feature of Co_3O_4 anode. As was reported, the long voltage plateau around 1.1 V is associated to a conversion from Co_3O_4 to $\text{Li}_x\text{Co}_3\text{O}_4$ or CoO , and then to Co during the lithium insertion process [16,45]. According to the literature, the plateau voltage in the galvanostatic charge–discharge curves was different from the potential in the CV curves in the first cycle, which may be related to the incomplete decomposition of the Co_3O_4 [45b]. The initial discharge and charge capacities are 1670.8 and $1341.3 \text{ mAh g}^{-1}$, respectively. The irreversible capacity loss for the first cycle is mainly attributed to the irreversible loss of lithium due to the formation of a solid electrolyte interface (SEI) film and the formation of amorphous Li_2O [46,47]. However, it is interesting to observe that after 60 cycles, the electrode still delivers reversible capacity as high as $1667.6 \text{ mAh g}^{-1}$, which is comparable to the initial discharge capacity of $1670.8 \text{ mA h g}^{-1}$, and even twice the theoretical prediction value for bulk Co_3O_4 (890 mAh g^{-1}). This phenomenon may

be attributed to the porous structure of Co_3O_4 and the formation of surface polymeric layer due to the decomposition of the electrolyte [17,48]. According to the literature, the surface polymeric layer is beneficial for the preserving of the mesoporous structure during discharge–charge processes, which can provide short path length with less resistance for the transporting of Li ions and electrons within electrolyte, and thus the electrochemical performance can be greatly improved [49]. Besides, to further investigate the electrochemical reactions of mesoporous Co_3O_4 nanobundles, cycle voltammetry (CV) was performed in the range of 0.01–3.00 V vs. Li^+/Li at a scan rate of 0.5 mV s^{-1} (Fig. 5b). In the first cycle, an irreversible peak with a maximum at around 0.66 V was observed, which can be attributed to the initial reduction in Co_3O_4 to Co , and irreversible reactions with the electrolyte [16,50–52]. Another dominant peak at 2.18 V was ascribed to the oxidation (delithiation) reaction, i.e. the formation of CoO . These two processes can be described by the electrochemical conversion reactions as follows:



Compared to the initial cycle, the reduction peak occurs an obvious shift toward the positive direction with the potential from 0.66 to 0.90 V and the peak intensity decreases evidently in the subsequent cycle, while the oxidation peak keeps constant. It is striking to note that the peak intensity and integral areas of the third cycle are completely same as that of the second one, indicating an excellent cycle stability of the mesoporous Co_3O_4 nanobundles.

Fig. 5c displays the cycle performance of the electrode made by mesoporous Co_3O_4 nanobundles at a current density of 0.1 A g^{-1} . The initial reversible capacity is up to $1670.8 \text{ mAh g}^{-1}$ and the initial Coulombic efficiency is 80.3%. It is interesting to observe that the capacity gradually increases from the second cycle and it can reach to $1667.6 \text{ mAh g}^{-1}$ after 60 cycles, which corresponds to 99.8% of the initial capacity and is about 4.5 times larger than the theoretical capacity of graphite (372 mAh g^{-1}). The gradual increase of the capacity from second cycle is common in porous materials and cobalt-based materials [6,9,17,48,53]. According to previous reports, [16,17,49] the reason may be attributed to the gradual activation of the pores. In our experiments, the existing of pores leads to the gradual access of more electrolytes into the pores of the electrode materials, which results in the capacity increasing during discharge–charge processes. In addition, even at higher current densities of 0.5 (tested after 10 cycles at 0.1 A g^{-1}), 1, and 5 A g^{-1} , the reversible capacities of $1492.4 \text{ mAh g}^{-1}$, $1264.8 \text{ mAh g}^{-1}$ and 603.0 mAh g^{-1} are retained after 100 cycles, respectively (Fig. 5d). This performance is much better than the reported Co_3O_4 -based materials with different morphologies (Table 1).

Furthermore, we also evaluated the rate capability of the mesoporous Co_3O_4 nanobundle electrode at different current densities (from 0.1 to 20 A g^{-1}), because the rate capability is an important parameter for practical applications of LIBs, for example, especially for electric vehicles and power tools. As shown in Fig. 5e, the Co_3O_4 nanobundle electrode exhibits outstanding rate capability with average discharge capacities of 1468, 1473, 1451, 1383, 1292, 1052, 735, and 367 mAh g^{-1} at current densities of 0.1, 0.2, 0.5, 1, 2, 5, 10, and 20 A g^{-1} , respectively. It can be clearly seen that even at the current density as high as 20 A g^{-1} , 367 mAh g^{-1} of the capacity is retained, which is still comparable to that of commercially used graphite. More importantly, while altering the current density back to 0.1 A g^{-1} , a discharge capacity of as high as 1713 mAh g^{-1} could be recovered, which is even higher than the initial reversible capacity. This result indicates the good reversibility of the

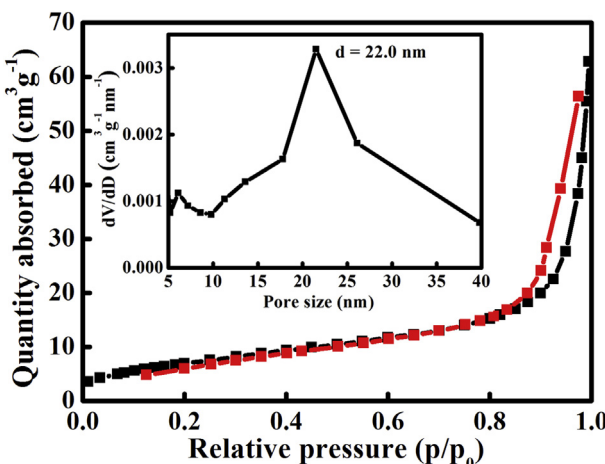


Fig. 4. Nitrogen adsorption–desorption isotherms and pore size distribution curve of the mesoporous Co_3O_4 hierarchical nanobundles.

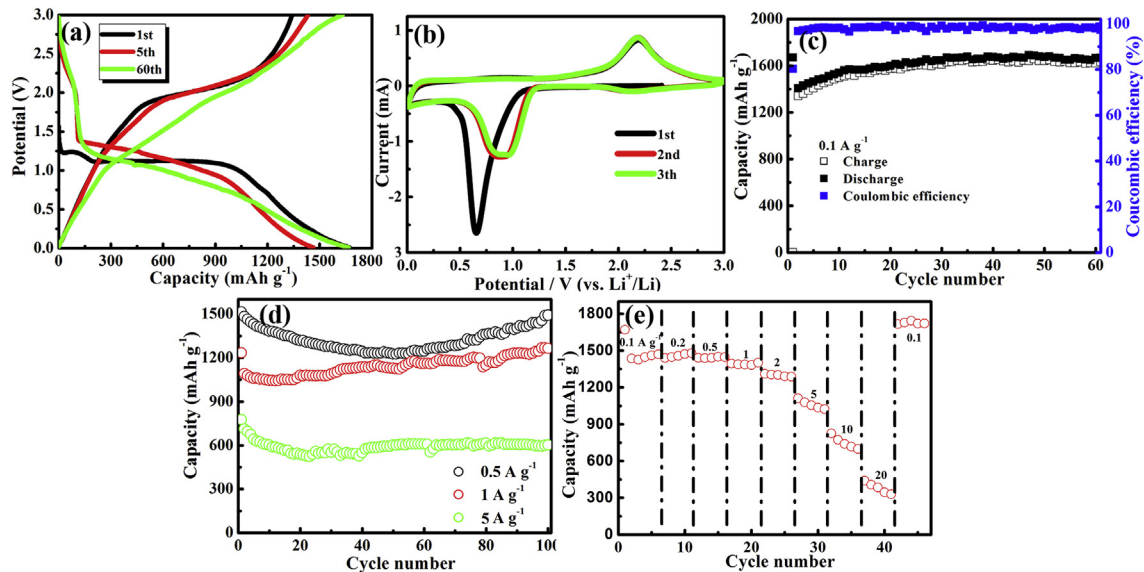


Fig. 5. (a) Discharge and charge profiles of the Co_3O_4 bundles at a current density of 0.1 A g^{-1} between 0.01 and 3.00 V for the first, fifth, and sixtieth cycles. (b) The first three cyclic voltammograms of the Co_3O_4 products. (c) Capacity vs. cycle number and the corresponding Columbic efficiency of Co_3O_4 at a current density of 0.1 A g^{-1} . (d) Cycle performance of the products at a current densities of 0.5 A g^{-1} , 1 A g^{-1} and 5 A g^{-1} , respectively. (e) Rate performance of the Co_3O_4 bundles at a current density from 0.1 A g^{-1} – 20 A g^{-1} .

materials, which may be ascribed to the nanometer-sized subunits and the activation of the pores [54,55]. To further confirm excellent stability of this structure, we tested the morphology by SEM and composition by XPS of the materials after 60 cycles at a current density of 0.1 A g^{-1} . SEM examination (Fig. S2a) for the electrode after 60 cycles (at discharged state) reveals that the original morphology of the Co_3O_4 is perfectly retained, confirming the superior structural stability. The Co XPS spectrum recorded on the discharged electrode confirms the existence of Co_3O_4 phase (Fig. S2b), but the peaks were weak, which was probably due to the coverage of a relatively thick SEI film on the surface of the electrode after prolonged cycling. Generally, the high rate capability of materials is especially desirable for LIBs, which can greatly reduce the charge/discharge time in practical applications. From this point of view, the excellent rate capability demonstrates that the mesoporous Co_3O_4 nanobundles in present study have a great potential

as a high-rate anode materials in LIBs. To the best of our knowledge, this is the first report on the capacity of Co_3O_4 at such high current densities.

Moreover, the influence of C additive (acetylene black) can be neglected in our investigation due to its small capacity contribution ($\sim 5\%$ of the total capacity). As displayed in the Fig. S3, we tested the cycling performance of the samples at a current density of 0.1 A g^{-1} under the conditions similar to the as-obtained Co_3O_4 except the absence of Co_3O_4 (a) and the substituting of Co_3O_4 by acetylene black in the same ratio (b). Both of the two results indicated the poor performance of the C additive. As one component of the electrode, its conductivity effect is more considered as an important factor for the final performance than its capacity effect.

According to above results, we know that the outstanding high-rate performance of the mesoporous Co_3O_4 hierarchical nanobundles is almost the best among the reported Co_3O_4 materials. Based on studies reported previously, we believe the high capacity and rate capability of the mesoporous Co_3O_4 hierarchical nanobundles undoubtedly result from their unique hierarchical mesoporous structure. This kind of structure in present study is exactly beneficial to the kinetics of the redox reactions, i.e. lithium ion and electron diffusion to/from the electrolyte/particle interface (Fig. 6a). More specifically, first, compared to nanoparticles, the one-dimensional nanobelt building blocks that consist of the Co_3O_4 hierarchical nanobundles can ensure a high electron transfer rate; because relatively few grain boundaries exist in the single nanobelt, which can greatly reduce trap numbers during the electron transport process. Second, the slip pores between neighboring nanobelts can effectively increase the diffusion coefficients and thus they allow for the full diffusion of the electrolyte, which is particularly important for current LIBs' applications with high-power requirements. Third, the mesopores running through the whole nanobelts will provide more interfacial bonding for extra active sites of Li^+ insertion, enhance the electrolyte/ Co_3O_4 contact area, shorten the lithium ion diffusion length in the nanobelts, and accommodate the strain induced by the volume change during the electrochemical reaction. It is because of these unique features that our mesoporous Co_3O_4 hierarchical nanobundles achieve high capacity, good cycle ability and high rate capability.

Table 1

Comparison of the cycle capacity of Co_3O_4 nanostructures with different morphologies.

Samples	a Current density (mA g^{-1})	b Cycle number	c Capacity (mAh g^{-1})	d Capacity (mAh g^{-1}) at high rate (mA g^{-1})
Co_3O_4 octahedrons [7]	100 (1000)	50	946 (714)	700 (2000)
Co_3O_4 hexapods [9]	100 (500)	40 (40)	800 (440)	–
$\text{Co}_3\text{O}_4/\text{C}$ quasi-spheres [10b]	170	20	1150	150 (10200)
$\text{Co}_3\text{O}_4/\text{GR}$ [11]	50	50	1004	787 (1000)
Co_3O_4 hollow spheres [14]	178	50	866	500.8 (1780)
Co_3O_4 nanobelts [15]	40	20	1400	<300 (890)
Co_3O_4 nanocages [17]	300	50	1465	535 (9000)
Co_3O_4 flowers [18]	100	100	694	–
Co_3O_4 branched wires [19]	100	50	1043	–
Co_3O_4 belts [6]	100 (1000)	60	980 (614)	605 (3000)
Co_3O_4 nanowires [50]	300	25	1050	–
$\text{Co}_3\text{O}_4/\text{CNTs}$ [51]	200	100	776	600 (1000)
This work	100 (1000)	60 (100)	1668(1265)	367 (20000)

Note: The current density values in brackets in row a corresponds to the cycles in brackets in row b and the capacity values in brackets in row c.

The current density values in brackets in row d corresponds to the capacity values in brackets in row d.

In order to further understand the transport kinetics for the mesoporous Co_3O_4 hierarchical nanobundles, electrochemical impedance spectroscopy (EIS) measurements were performed from 100 KHz to 0.01 Hz, as shown in Fig. 6b,c. The measured EIS spectra are analyzed and fitted and an equivalent circuit for this cell system is shown in Fig. 7. Fig. 6b,c show the EIS spectra of the electrodes after different cycles at discharge state at a current density of 0.1 A g^{-1} , and the electrodes at different current densities after same cycles, respectively. The Nyquist plots all consist of a depressed semicircle in the high-middle frequency regions and the straight line in the low-frequency region. The semicircle at high frequency corresponds to the electrolyte resistance (R_s), while that at high-middle frequencies can be assigned to the SEI film and contact resistance (R_f), and the charge-transfer impedance on electrode–electrolyte interface (R_{ct}). It is interesting to observe that almost for all EIS spectra, the linear region has two different slopes. The smaller slope part of the linear region should correspond to diffusion barrier layer impedance (R_{zt}) and the larger slope part may be ascribed to the semi-infinite diffusion of the Li-ions in the Co_3O_4 electrodes (Warburg impedance, Z_w) [56]. Based on previous lithium storage mechanism of Co_3O_4 , in the discharge state, the electrode was mainly composed of Co and Li_2O , which resulted in the formation of barrier layers. For the EIS spectra of the electrodes after different cycles at discharge state at a current density of 0.1 A g^{-1} (Fig. 6b), in contrast to most of reports that the cell impedance increases with increasing cycle number, the diameter of the semicircle at high-middle frequencies decreases obviously with increasing cycle number, indicating depressed R_f and R_{ct} resistances. This interesting phenomenon is in well agreement with few reports [57]. The possible reason may be related to the stabilization of the SEI layer during cycling and the mesoporous hierarchical structure of Co_3O_4 , allowing for the diffusion of electrolyte into the pores more easily and facilitating facial charge transfer at the nanoscale unit/electrolyte interface. Even more striking is that for the electrodes after same cycles but at different current

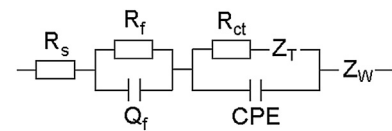


Fig. 7. Equivalent circuit for fitting experimental EIS data.

densities (Fig. 6b), the diameter of the semicircle at high-middle frequencies also decreases obviously with increasing the current density (Fig. 6c). This result definitely demonstrates that the mesoporous Co_3O_4 hierarchical nanobundles in our case are indeed suitable for high-rate discharge/charge process, which is in well agreement with previous rate performance test.

4. Conclusions

In summary, we have designed a facile strategy to fabricate mesoporous Co_3O_4 hierarchical nanobundles, which are obtained by a hydrothermal method followed by an annealing process. The resultant materials exhibit high capacity and excellent rate capability when used as anode materials in LIBs. A discharge capacity as high as $1670.8 \text{ mAh g}^{-1}$ could be maintained at a current density of 0.1 A g^{-1} and even at the current density as high as 20 A g^{-1} , 367 mAh g^{-1} of the capacity is retained, which is still comparable to that of commercially used graphite. The excellent electrochemical performance should be attributed to the mesoporous hierarchical structure, which not only provide a short ion transport pathway but also increase electrode–electrolyte contact area for more Li^+ crossing the interface. The current strategy is low-cost, effective and environment friendly and it may be extended to prepare other transition metal oxide materials, which have wide applications in broad fields including sensors, absorption, catalysis and electrochemical capacitors.

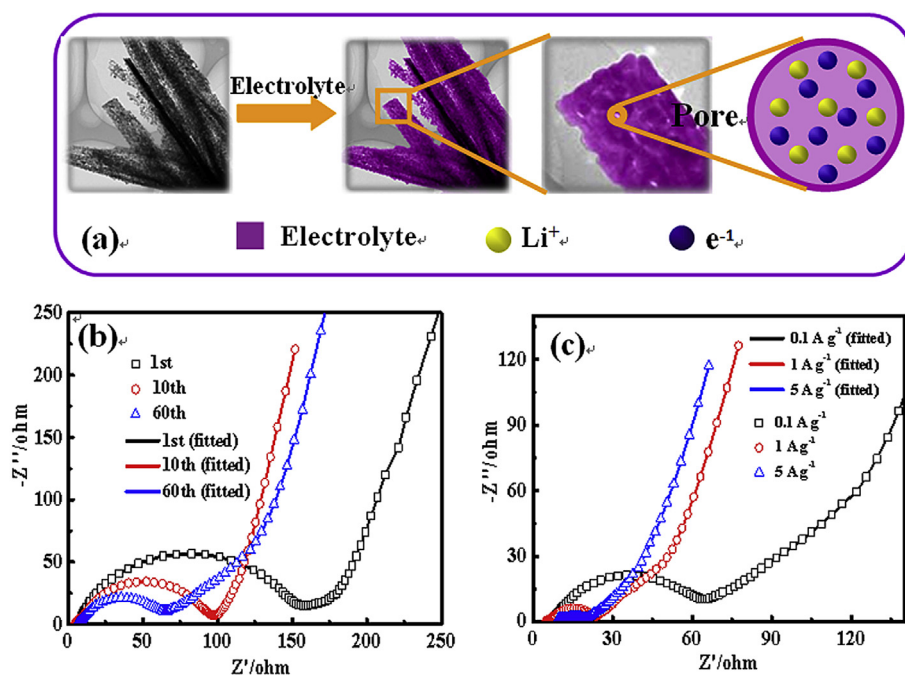


Fig. 6. (a) Schematic illustration of the diffusion of electrolyte, electron and Li^+ . Electrochemical impedance spectroscopies of the mesoporous Co_3O_4 hierarchical nanobundles: (b) after different cycles at discharged state at a current density of 0.1 A g^{-1} and (c) after 60 cycles at discharged state at different current densities. The fitting results are represented by the solid lines.

Acknowledgments

This work was financially supported by the National Natural Science Foundation of China 21173021, 21231002, 21276026, 21271023, 91022006, and 20973023, the 111 Project (B07012), the Program of Cooperation of the Beijing Education Commission (200901739006), and Specialized research fund for the doctoral program of higher education (SRFDP. No. 20101101110031).

Appendix A. Supplementary data

Supplementary data related to this article can be found at <http://dx.doi.org/10.1016/j.jpowsour.2013.08.069>.

References

- [1] N. Jayaprakash, W. Jones, S. Moganty, L. Archer, *J. Power Sources* 200 (2012) 53.
- [2] Y. Xiao, M. Cao, L. Ren, C. Hu, *Nanoscale* 4 (2012) 7469.
- [3] L. Zhou, D. Zhao, X. Lou, *Angew. Chem.* 124 (2012) 243.
- [4] C. Hu, Y. Xiao, Y. Zhao, N. Chen, Z. Zhang, M. Cao, L. Qu, *Nanoscale* 5 (2013) 2726.
- [5] K. Amine, I. Belharouak, Z. Chen, T. Tran, H. Yumoto, N. Ota, S. Myung, Y. Sun, *Adv. Mater.* 22 (2010) 3052.
- [6] H. Huang, W. Zhu, X. Tao, Y. Xia, Z. Yu, J. Fang, Y. Gan, W. Zhang, *ACS Appl. Mater. Interfaces* 4 (2012) 5974.
- [7] (a) X. Xiao, X. Liu, H. Zhao, D. Chen, F. Liu, J. Xiang, Z. Hu, Y. Li, *Adv. Mater.* 24 (2012) 5762;
(b) L. Tao, J. Zai, K. Wang, H. Zhang, M. Xu, J. Shen, Y. Su, X. Qian, *J. Power Sources* 202 (2012) 230.
- [8] Y. Li, B. Tan, Y. Wu, *Nano Lett.* 8 (2008) 265.
- [9] L. Wang, B. Liu, S. Ran, H. Huang, X. Wang, B. Liang, D. Chen, G. Shen, *J. Mater. Chem.* 22 (2012) 23541.
- [10] (a) S. Yang, X. Feng, S. Ivanovici, K. Mllen, *Angew. Chem. Int. Ed.* 49 (2010) 8408;
(b) J. Liu, Y. Wan, C. Liu, W. Liu, S. Ji, Y. Zhou, J. Wang, *Eur. J. Inorg. Chem.* 3825 (2012) 3825.
- [11] (a) B. Choi, S. Chang, Y. Lee, J. Bae, H. Kim, Y. Huh, *Nanoscale* 4 (2012) 5924;
(b) A. Rai, J. Gim, L. Anh, J. Kim, *Electrochim. Acta* 100 (2013) 63.
- [12] J. Chen, X. Xia, J. Tu, Q. Xiong, Y. Yu, X. Wang, C. Gu, *J. Mater. Chem.* 22 (2012) 15056.
- [13] (a) J. Ma, A. Manthiram, *RSC Adv.* 2 (2012) 3187;
(b) Y. Yao, J. Zhang, T. Huang, H. Mao, A. Yu, *Int. J. Electrochem. Sci.* 8 (2013) 3302.
- [14] X. Wang, X. Wu, Y. Guo, Y. Zhong, X. Cao, Y. Ma, J. Yao, *Adv. Funct. Mater.* 20 (2010) 1680.
- [15] L. Tian, H. Zou, J. Fu, X. Yang, Y. Wang, H. Guo, X. Fu, C. Liang, M. Wu, P. Shen, Q. Gao, *Adv. Funct. Mater.* 20 (2010) 617.
- [16] S. Xiong, J. Chen, X. Lou, H. Zeng, *Adv. Funct. Mater.* 22 (2012) 861.
- [17] L. Hu, N. Yan, Q. Chen, P. Zhang, H. Zhong, X. Zheng, Y. Li, X. Hu, *Chem. Eur. J.* 18 (2012) 8971.
- [18] J. Chen, T. Zhu, Q. Hu, J. Gao, F. Su, S. Qiao, X. Lou, *ACS Appl. Mater. Interfaces* 2 (2010) 3628.
- [19] C. Li, X. Yin, L. Chen, Q. Li, T. Wang, *Appl. Phys. Lett.* 97 (2010) 043501.
- [20] M. Tiemann, *Chem. Eur. J.* 13 (2007) 8376.
- [21] G. Zhang, X. Shen, Y. Yang, *J. Phys. Chem. C* 115 (2011) 7145.
- [22] A. Stevanovic, J. Yates Jr., *Langmuir* 28 (2012) 5652.
- [23] H. Wang, L. Zheng, C. Liu, Y. Liu, C. Luan, H. Cheng, Y. Li, L. Martinu, J. Zapien, I. Bello, *J. Phys. Chem. C* 115 (2011) 10419.
- [24] J. Liu, H. Xia, L. Lu, D. Xue, *J. Mater. Chem.* 20 (2010) 1506.
- [25] Y. Wan, D. Zhao, *Chem. Rev.* 107 (2007) 2821.
- [26] X. Wang, W. Liu, J. Liu, F. Wang, J. Kong, S. Qiu, C. He, L. Luan, *ACS Appl. Mater. Interfaces* 4 (2012) 817.
- [27] L. Zhao, Y. Hu, H. Li, Z. Wang, L. Chen, *Adv. Mater.* 23 (2011) 1385.
- [28] L. Hu, H. Zhong, X. Zheng, Y. Huang, P. Zhang, Q. Chen, *Sci. Rep.* 2 (2012) 986.
- [29] A. Pan, H. Wu, L. Yu, T. Zhu, X. Lou, *ACS Appl. Mater. Interfaces* 4 (2012) 3874.
- [30] M. Ge, J. Rong, X. Fang, C. Zhou, *Nano Lett.* 12 (2012) 2318.
- [31] A. Arico, P. Bruce, B. Scrosati, J. Tarascon, W. Schalkwijk, *Nat. Mater.* 4 (2005) 366.
- [32] J. Cai, Z. Li, P. Shen, *ACS Appl. Mater. Interfaces* 4 (2012) 4093.
- [33] N. Yan, F. Wang, H. Zhong, Y. Li, Y. Wang, L. Hu, Q. Chen, *Sci. Rep.* 3 (2013) 1568.
- [34] H. Liu, D. Su, R. Zhou, B. Sun, G. Wang, S. Qiao, *Adv. Energy Mater.* 2 (2012) 970.
- [35] G. Jia, M. Yang, Y. Song, H. You, H. Zhan, *Cryst. Growth Des.* 9 (2009) 301.
- [36] B. Alken, W. Hsu, E. Matijevic, *J. Am. Ceram. Soc.* 71 (1988) 845.
- [37] S. Hwang, A. Umar, S. Kim, S. Al-Sayari, M. Abaker, A. Al-Hajry, A. Stephan, *Electrochim. Acta* 56 (2011) 8534.
- [38] (a) B. Duan, Q. Cao, *Electrochim. Acta* 64 (2012) 154;
(b) N. Yan, L. Hu, Y. Li, Y. Wang, H. Zhong, X. Hu, X. Kong, Q. Chen, *J. Phys. Chem. C* 116 (2012) 7227.
- [39] C. Li, X. Yin, Q. Li, L. Chen, T. Wang, *Chem. Eur. J.* 17 (2011) 1596.
- [40] L. Zhang, X. Zhao, W. Ma, M. Wu, N. Qian, W. Lu, *CrystEngComm* 15 (2013) 1389.
- [41] Y. Wang, H. Xia, L. Lu, J. Lin, *ACS Nano* 4 (2010) 1425.
- [42] J. Xiao, S. Yang, *RSC Adv.* 1 (2011) 588.
- [43] D. Larcher, G. Sudant, J. Leriche, Y. Chabre, J. Tarascon, *J. Electrochem. Soc.* 149 (2002) A234.
- [44] W. Yao, J. Yang, J. Wang, Y. Nuli, *J. Electrochem. Soc.* 155 (2008) A903.
- [45] (a) P. Poizot, S. Laruelle, S. Grugeon, L. Dupont, J. Tarascon, *Nature* 407 (2000) 496;
(b) N. Du, H. Zhang, B. Chen, J. Wu, X. Ma, Z. Liu, Y. Zhang, D. Yang, X. Huang, J. Tu, *Adv. Mater.* 19 (2007) 4505.
- [46] N. Munichandraiah, L. Scanlon, R. Marsh, *J. Power Sources* 72 (1998) 203.
- [47] J. Li, S. Xiong, Y. Liu, Z. Ju, Y. Qian, *ACS Appl. Mater. Interfaces* 5 (2013) 981.
- [48] (a) G. Zhou, D. Wang, F. Li, L. Zhang, N. Li, Z. Wu, L. Wen, G. Lu, H. Cheng, *Chem. Mater.* 22 (2010) 5306;
(b) W. Mei, J. Huang, L. Zhu, Z. Ye, Y. Mai, J. Tu, *J. Mater. Chem.* 22 (2012) 9315;
(c) L. Qie, W. Chen, Z. Wang, Q. Shao, X. Li, L. Yuan, X. Hu, W. Zhang, Y. Huang, *Adv. Mater.* 24 (2012) 2047.
- [49] (a) D. Su, M. Ford, G. Wang, *Sci. Rep.* 2 (2012) 924;
(b) G. Binotto, D. Larcher, A. Prakash, R. Urbina, M. Hegde, J. Tarascon, *Chem. Mater.* 19 (2007) 3032;
(c) S. Needham, G. Wang, K. Konstantinov, Y. Tournayre, Z. Lao, H. Liu, *Electrochim. Solid State Lett.* 9 (2006) A315.
- [50] W. Zhou, C. Cheng, J. Liu, Y. Tay, J. Jiang, X. Jia, J. Zhang, H. Gong, H. Hng, T. Yu, H. Fan, *Adv. Funct. Mater.* 21 (2011) 2439.
- [51] S. Chou, J. Wang, H. Liu, S. Dou, *J. Power Sources* 182 (2008) 359.
- [52] C. Li, X. Yin, L. Chen, Q. Li, T. Wang, *Chem. Eur. J.* 16 (2010) 5215.
- [53] Y. Mao, H. Duan, B. Xu, L. Zhang, Y. Hu, C. Zhao, Z. Wang, L. Chen, Y. Yang, *Energy Environ. Sci.* 5 (2012) 7950.
- [54] L. Zhuo, Y. Wu, J. Ming, L. Wang, Y. Yu, X. Zhang, F. Zhao, *J. Mater. Chem. A* 1 (2013) 1141.
- [55] (a) X. Xu, R. Cao, S. Jeong, J. Cho, *Nano Lett.* 12 (2012) 4988.
- [56] C. Cao, J. Zhang, *An Introduction to Electrochemical Impedance Spectroscopy*, Science, Beijing, 2002, pp. 86–106.
- [57] (a) Y. Liu, C. Mi, L. Su, X. Zhang, *Electrochim. Acta* 53 (2008) 2507;
(b) Y. Liu, X. Zhang, *Electrochim. Acta* 54 (2009) 4180;
(c) D. Su, H. Kim, W. Kim, G. Wang, *Chem. Eur. J.* 18 (2012) 8224.